Ultrafast Charge Separation and Indirect Exciton Formation in a MoS_2—$MoSe_2$ van der Waals Heterostructure

Frank Ceballos, Matthew Z. Bellus, Hsin-Ying Chiu,* and Hui Zhao*

Department of Physics and Astronomy, The University of Kansas, Lawrence, Kansas 66045, United States

ABSTRACT We observe subpicosecond charge separation and formation of indirect excitons a van der Waals heterostructure formed by molybdenum disulfide and molybdenum diselenide monolayers. The sample is fabricated by manually stacking monolayer MoS_2 and $MoSe_2$ flakes prepared by mechanical exfoliation. Photoluminescence measurements confirm the formation of an effective heterojunction. In the transient absorption measurements, an ultrafast laser pulse resonantly injects excitons in the $MoSe_2$ layer of the heterostructure. Differential reflection of a probe pulse tuned to the MoS_2 exciton resonance is immediately observed following the pump excitation. This proves ultrafast transfer of electrons from $MoSe_2$ to MoS_2 layers, despite the strong Coulomb attraction from the holes in the resonantly excited excitons. Conversely, when excitons are selectively injected in MoS_2, holes transfer to $MoSe_2$ on an ultrafast time scale, too, as observed by measuring the differential reflection of a probe tuned to the $MoSe_2$ resonance. The ultrafast charge transfer process is followed by the formation of spatially indirect excitons with electrons and holes residing in different layers. The lifetime of these indirect excitons are found to be longer than that of the direct excitons in individual MoS_2 and $MoSe_2$ monolayers.

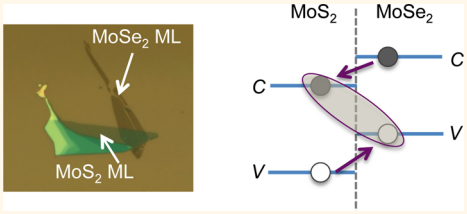

KEYWORDS: van der Waals heterostructure · transition metal dichalcogenides · molybdenum disulfide · molybdenum diselenide · 2D materials · transient absorption · exciton

For several decades, heterostructures formed by interfacing two different materials have been a cornerstone for developing functional materials with emergent properties.[1−4] Traditionally, such structures are fabricated by epitaxy techniques that require lattice matching of the component materials. Hence, the selection of component materials is restricted to those with similar lattice structures, where oftentimes, a slight lattice mismatch results in poor interface qualities. The newly developed two-dimensional crystals from layered materials, such as graphene,[5,6] boron nitride,[7] and transition metal dichalcogenides (TMDs),[8] open up a new avenue for fabricating the so-called van der Waals heterostructures.[9] Since the weak van der Waals interlayer coupling is used, the lattice-matching requirement is relaxed. Thus, a huge number of combinations can be designed and explored.[10] The interface can be atomically sharp and the junction region can be as thin as two atomic layers.[11] In addition, these van der Waals heterostructures are flexible and their fabrication is compatible with current thin-film technologies. The process can potentially be scaled up to make multilayers or even three-dimensional crystals.[12]

So far, most studies on van der Waals heterostructures focus on those formed between graphene and multilayer TMDs. Vertical tunneling transistors utilizing a multilayer MoS_2 or WS_2 as the tunneling barrier between graphene layers have achieved high on—off ratios.[13−20] The tunneling can be controlled by inserting an insulating layer between MoS_2 and graphene, as demonstrated in memory devices.[17,21] These structures also showed promising applications in optoelectronics,[22] since they can potentially combine the novel optical properties of TMDs with the superior transport properties of graphene.[23−29] Very recently, direct growth of various TMD films on graphene has also been demonstrated.[30−32]

* Address correspondence to chiu@ku.edu, huizhao@ku.edu.

Received for review October 9, 2014 and accepted November 17, 2014.

Published online November 17, 2014
10.1021/nn505736z

Compared to these semimetal−semiconductor structures, all-semiconducting heterostructures formed by different members of TMDs are closer in concept to traditional semiconducting heterostructures. When used as active layers in optoelectronic devices, they can potentially overcome some limitations of individual TMD layers. For example, one challenge in using individual TMD films in photovoltaic devices is their relatively low light absorption. Although monolayer (ML) TMDs can absorb more than 10% of incident light,[22] such a high absorption coefficient cannot be scaled up by increasing the thickness, owing to the direct-to-indirect bandgap transition in multilayers.[33,34] However, thanks to the weak interlayer coupling, TMD monolayers in heterostructures maintain their own direct bandstructures.[35,36] Hence, their absorption is expected to simply add up.[22] Furthermore, based on first-principles calculations, most heterostructures formed by two TMD monolayers have type-II band alignments, where the bottom of the conduction band and the top of the valence band reside in different layers.[37−42] Such a band alignment is expected to facilitate the spatial separation of electrons and holes after photoexcitation, which can be utilized in photovoltaic devices. It can also result in longer lifetime of photocarriers due to the spatial separation of electrons and holes. In recent experiments on MoS_2−WSe_2 heterostructures, quenching of photoluminescence (PL) was observed,[43] which indicates the interlayer charge transfer, and their applications in photovoltaic[44] and field effect transistors[45] were demonstrated. Very recently, ultrafast hole transfer from MoS_2 to WS_2[46] and long lifetimes of indirect excitons in a $MoSe_2$−WSe_2 heterostructure were revealed.[47]

We report direct time-resolution of charge separation and indirect exciton formation in a heterostructure formed by MoS_2 and $MoSe_2$ MLs by transient absorption measurements. By selectively injecting excitons in one of the layers and probing the exciton states of the other layer, we find that electrons and holes transfer to the lower-energy side of the heterostructure on a subpicosecond time scale. Once transferred, electrons and holes form spatially indirect excitons, which have longer recombination lifetimes than excitons in individual MLs.

RESULTS AND DISCUSSION

We make MoS_2 [Figure 1a] and $MoSe_2$ [Figure 1b] MLs by mechanical exfoliation of bulk crystals. The MoS_2−$MoSe_2$ heterostructure sample [Figure 1c] is fabricated by transferring the MoS_2 ML onto the $MoSe_2$ ML on a Si-SiO_2 substrate. Figure 1d illustrates the predicted band alignment of the heterostructure,[37,38] where the lowest conduction band (*C*) and the highest valence band (*V*) lie in MoS_2 and $MoSe_2$ layers, respectively. The offset of the conduction (valence) band is predicted to be about 0.37 (0.63) eV.[37,38] In addition to

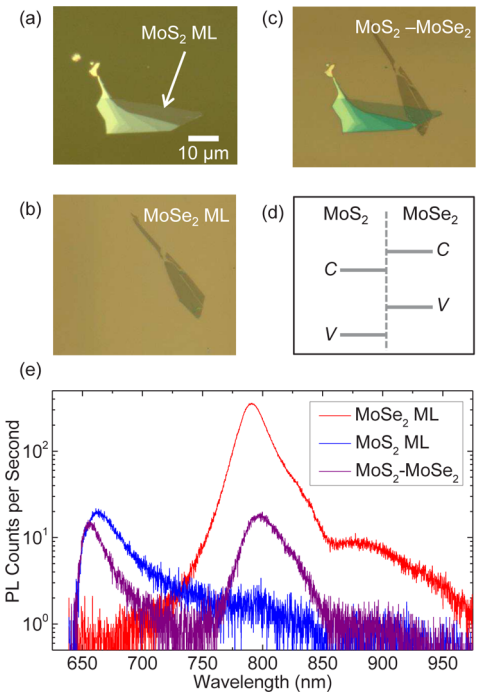

Figure 1. (a) Optical microscope image of a MoS_2 flake that contains a monolayer (ML) region. (b) A $MoSe_2$ ML on a Si-SiO_2 substrate. (c) The MoS_2−$MoSe_2$ heterostructure fabricated by transferring the MoS_2 flake shown in (a) to the top of the $MoSe_2$ ML shown in (b). (d) The predicted alignment of the conduction (*C*) and valence (*V*) bands of the heterostructure. (e) Photoluminescence (PL) spectra measured from the regions of the MoS_2 ML (blue), the $MoSe_2$ ML (red), and the heterostructure (purple).

the heterostructure region, this flake also contains regions of individual MLs of MoS_2 and $MoSe_2$, and hence facilitates direct comparison of the heterostructure with the individual MLs.

Figure 1e shows the PL spectra of the MoS_2 ML (blue), $MoSe_2$ ML (red), and MoS_2−$MoSe_2$ heterostructure (purple) regions under the excitation of a 632.8 nm continuous-wave laser with an incident power of about 50 μW. The peak positions of the MoS_2 (663.0 nm) and $MoSe_2$ (790.5 nm) MLs are consistent with previously reported values.[33,34,48−50] The PL yield of the $MoSe_2$ ML is about 20 times higher than that of the MoS_2 ML, suggesting stronger nonradiative recombination in the latter. The spectrum of the heterostructure has two peaks at 656.0 and 798.5 nm that are close to the peaks of the individual MoS_2 and $MoSe_2$ MLs, respectively. This confirms that the exciton states of the individual layers are largely unchanged in the heterostructure.[35,36] We attribute the small shifts of 7−8 nm of these peaks to the different dielectric environments in the heterostructure compared to the individual MLs. The PL peak of $MoSe_2$ in the heterostructure is lower than the individual $MoSe_2$ ML by about 20 times. Such a pronounced PL quenching effect suggests that in the heterostructure most electrons excited in $MoSe_2$ transfer to the lower states in MoS_2, instead of forming excitons in $MoSe_2$ and recombine radiatively. Similar

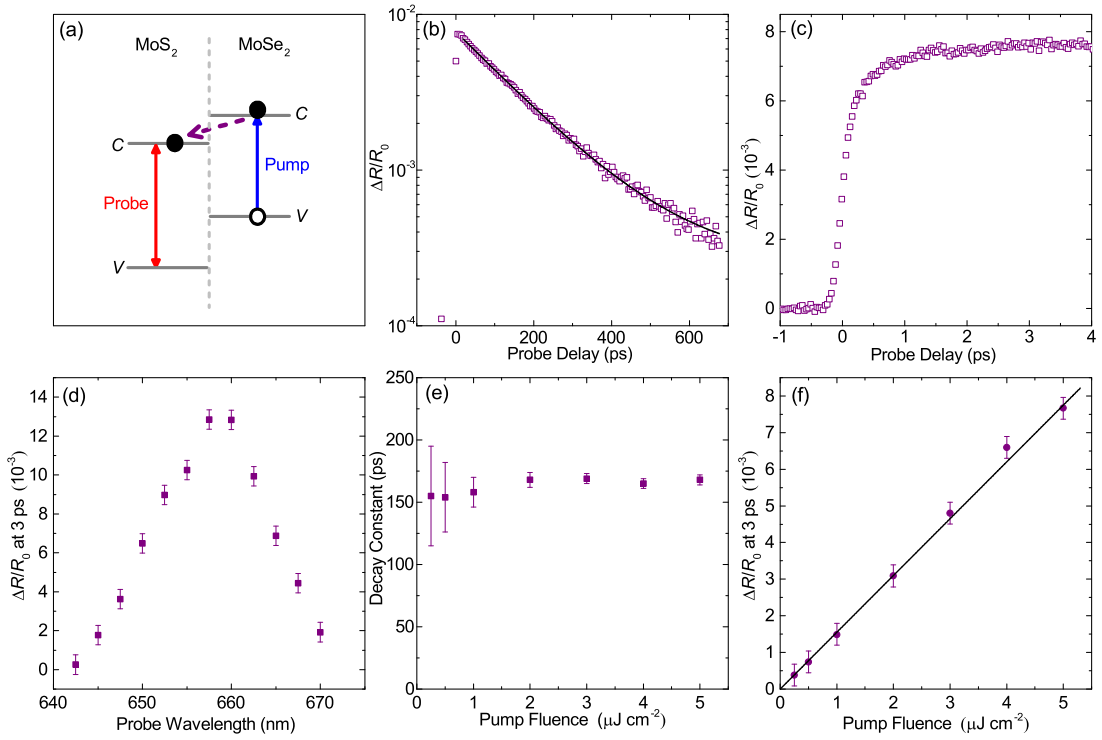

Figure 2. (a) Schematics of the pump−probe configuration used to study the transfer of electrons from $MoSe_2$ to MoS_2 in the heterostructure. (b) Differential reflection signal as a function of the probe delay. The black line is a single-exponential fit (with a baseline). (c) Differential reflection signal near zero probe delay. (d) The magnitude of the differential reflection signal as a function of the probe wavelength. (e) Decay constant of the differential reflection signal as a function of the pump fluence, deduced from single-exponential fits to the signal measured under different values of the pump fluence. (f) The magnitude of the differential reflection signal as a function of the pump fluence. The black line indicates a linear fit.

PL quenching effect has been recently observed in MoS_2−WSe_2 heterostructures.[43,44] In contrast, the peak of the MoS_2 ML is only decreased by about 30% in the heterostructure sample. We attribute this to the pronounced nonradiative recombination in MoS_2, which is also consistent with the low PL yield of the MoS_2 ML compared to the $MoSe_2$ ML. We note that the transition from the conduction band of MoS_2 to the valence band of $MoSe_2$ in the heterostructure is expected to be at about 1030 nm,[37,38] which is out of the spectral range of this study.

To study the dynamics of charge transfer, exciton formation, and exciton recombination in the MoS_2−$MoSe_2$ heterostructure, we perform ultrafast transient absorption measurements in reflection geometry.

First, we study transfer of electrons from the $MoSe_2$ to the MoS_2 layers, with a configuration illustrated in Figure 2a. A 100 fs pump pulse with a central wavelength of 790 nm is used to excite the sample. Since it is tuned to the exciton resonance of the $MoSe_2$ layer and is far below any exciton states of MoS_2, the pump pulse selectively injects excitons in the $MoSe_2$ layer (blue vertical line). A 655 nm probe pulse is tuned to the exciton resonance of the MoS_2 layer (red vertical line). Differential reflection of this pulse is measured as a function of the time delay of the probe pulse with respect to the pump pulse, in order to monitor the transient absorption of this exciton resonance. Here the differential reflection is defined as the normalized change of the reflectance caused by the pump, $\Delta R/R_0 \equiv (R - R_0)/R_0$, where R and R_0 are the reflectance of the sample with and without the presence of the pump pulse, respectively.

Panels b and c of Figure 2 show the differential reflection signal on long and short time ranges, respectively, measured with a pump energy fluence of 5 μJ cm^{-2}. Since the probe pulse detects the MoS_2 layer, which is not excited by the pump, a signal is expected only if electrons injected in $MoSe_2$ transfer to MoS_2 across the van der Waals interface, as illustrated by the purple dashed line in Figure 2a. As shown in Figure 2c, the signal reaches the maximum level on an ultrashort time scale. This indicates that the electrons injected in $MoSe_2$ transfer to MoS_2 layer rapidly, despite the strong Coulomb interaction between electrons and holes in the injected excitons. The decay of the signal is single exponential, as indicated by the black line in Figure 2b, with a time constant of about 160 ps. We note that the positive sign of the signal indicates that the pump-injected carriers cause an increase of the probe reflection. To exclude the possibility that the probe detects the $MoSe_2$ layer *via* interacting with higher-energy states in $MoSe_2$, we repeat the measurement with different probe wavelengths. As summarized in Figure 2d, the magnitude of the signal depends strongly on the probe

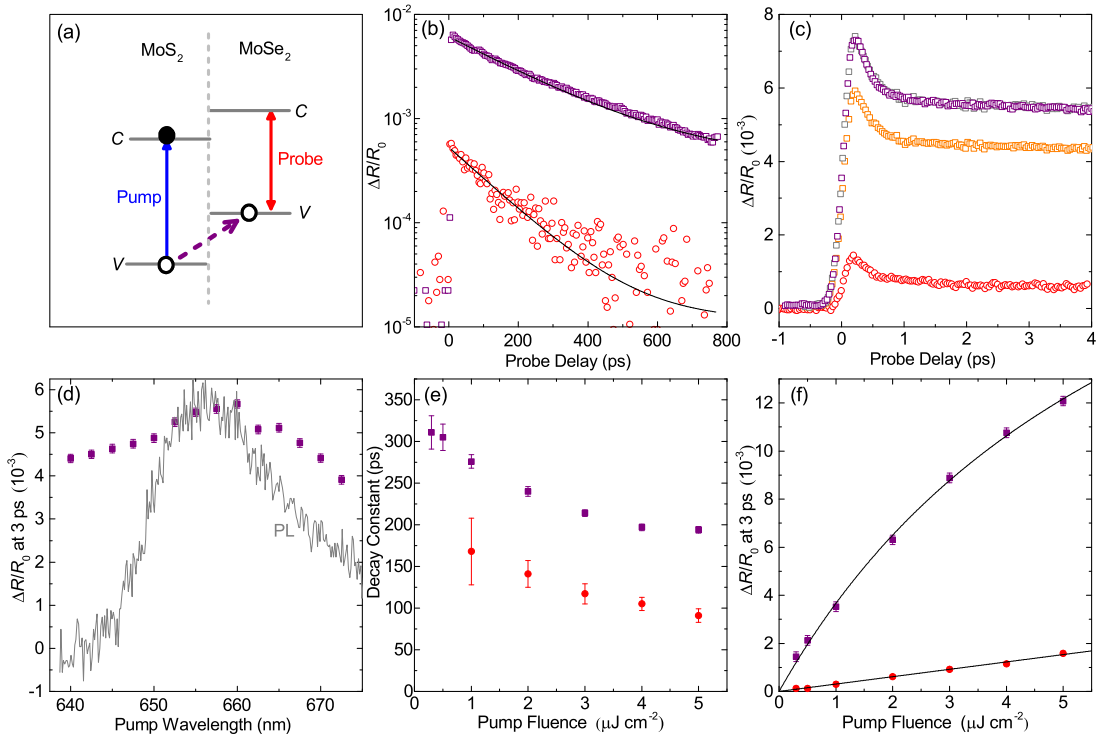

Figure 3. (a) Schematics of the pump−probe configuration used to study the transfer of holes from MoS_2 to $MoSe_2$ in the heterostructure. (b) Differential reflection signal as a function of the probe delay measured from the heterostructure (purple squares) and the $MoSe_2$ ML regions (red circles). The black lines are single-exponential fits. (c) Differential reflection signal near zero probe delay. The purple and orange squares are measured with pump wavelengths of 655 and 670 nm, respectively. The gray squares are scaled from the orange squares. The red circles are measured from the $MoSe_2$ ML. (d) The magnitude of the differential reflection signal from the heterostructure as a function of the pump wavelength (purple squares) and the PL spectrum of the heterostructure (gray line). (e) Decay constants of the differential reflection signal as a function of the pump fluence of the heterostructure (purple squares) and the $MoSe_2$ ML regions (red circles), respectively. These values are deduced from single-exponential fits to the signal measured under different values of the pump fluence. (f) The magnitude of the differential reflection signal from the heterostructure (purple squares) and the $MoSe_2$ ML regions (red circles) as a function of the pump fluence.

wavelength, with a peak similar to the MoS_2 PL from the heterostructure sample [Figure 1e]. This confirms that the differential reflection signal is mainly from the exciton resonance of MoS_2. By repeating the measurement with various values of the pump fluence, we find that the decay constant is independent of the pump fluence, as shown in Figure 2e, while the magnitude of the signal is proportional to the pump fluence [Figure 2f].

Next, we study the transfer of holes from MoS_2 to $MoSe_2$ by using a configuration illustrated in Figure 3a. Here, we resonantly inject excitons in the MoS_2 layer with a 655 nm pump pulse (blue vertical arrow), and probe the $MoSe_2$ exciton resonance with a 790 nm pulse (red vertical arrow). The differential reflection signal measured with a pump fluence of 2 μJ cm^{-2} is plotted as the purple squares in panels b and c of Figure 3 for two different time ranges. The signal rises to a peak quickly, and then decays single-exponentially (after a transient process of about 1 ps), with a time constant of about 240 ps (black line).

Unlike the previous configuration summarized in Figure 2, where the two layers are selectively pumped and probed, here the 655 nm pulse excites both layers. To separate the contributions of photocarriers injected in the two layers, we repeat the measurement with different pump wavelengths around the exciton resonance of MoS_2. The purple squares in Figure 3d show the magnitude of the signal. The PL spectrum of the heterostructure sample in this wavelength range is also plotted for comparison (gray line). Since the absorption of $MoSe_2$ varies slowly and monotonically in this wavelength range,[49,51] the observed pump-wavelength dependence confirms the contribution of the excitons injected in MoS_2 to the differential reflection signal. From the variation of the signal magnitude of about 30% in this range, we can roughly estimate that with a pump wavelength of 655 nm, the excitons injected in MoS_2 make a contribution of about 30%. As we change the pump wavelength in this range, and hence vary the relative contributions of the excitons injected in MoS_2 and those injected in $MoSe_2$, the same dynamics of the signal is observed. For example, the orange squares in Figure 3c shows the signal measured with a pump wavelength of 670 nm. After multiplied by a factor of 1.25 to match the magnitude (gray squares), its time variation perfectly matches the signal measured with the 655 nm pump. If the hole transfer from MoS_2 to

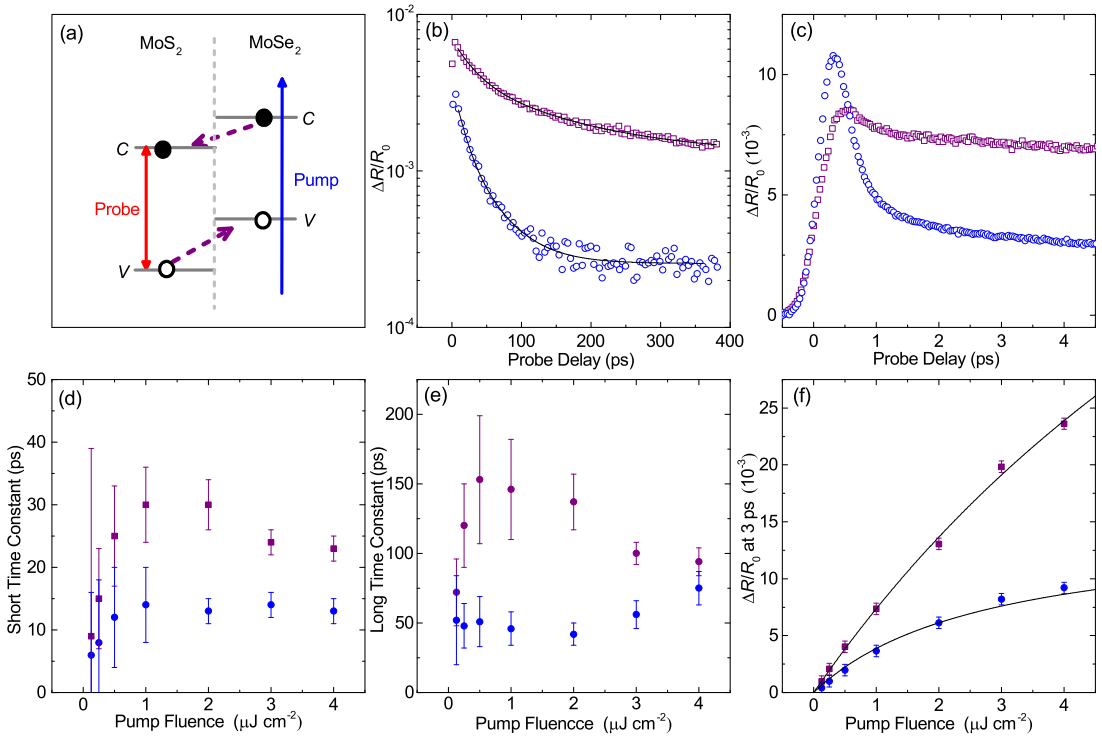

Figure 4. (a) Schematics of the pump−probe configuration with a 395 nm pump exciting both layers of the heterostructure (blue vertical arrow) and a 655 nm probe at the MoS_2 resonance (red vertical arrow). (b) Differential reflection signal as a function of the probe delay measured from the heterostructure (purple squares) and the MoS_2 ML (blue circles). The black lines are biexponential fits. (c) Same as (b) but near zero probe delay. (d) The short time constant of the differential reflection signal as a function of the pump fluence, deduced from biexponential fits of the decay curves from the heterostructure (purple squares) and the MoS_2 ML (blue circles). (e) Same as (d) but showing the slow time constants. (f) The magnitude of the differential reflection signal from the heterostructure (purple squares) and the $MoSe_2$ ML (blue circles) as a function of the pump fluence.

$MoSe_2$ were a slow process, a slow rising component should have been observed with the 655 nm pump. Hence, the observed same dynamics in this pump-wavelength range indicates that the holes injected in MoS_2 transfer to $MoSe_2$ [purple dashes arrow in Figure 3a] on a time scale comparable to, or shorter than, the time resolution of our setup of about 200 fs.

Once the holes transfer to the $MoSe_2$ layer, they are expected to form spatially indirect excitons with electrons in the MoS_2 layer. Hence, the decay of the differential reflection signal, with a time constant of about 240 ps, reflects the recombination lifetime of these indirect excitons. For comparison, we also measure the individual $MoSe_2$ ML under the same conditions. As shown as the red circles in panels b and c of Figure 3, the signal is about 10 times smaller than the heterostructure, and decays faster, with a time constant of about 150 ps. As we change the pump fluence, the decay of the signal from both samples remains single exponential. However, the decay constants decrease with the pump fluence, as shown in Figure 3e. The faster decay at higher density in each sample can be attributed to the influence of the exciton−exciton annihilation, which was recently observed in both $MoSe_2$ and MoS_2 MLs.[52,53] The decay is slower in the heterostructure sample, which confirms the longer lifetime of the indirect excitons owing to the slower recombination rate due to the spatial separation of electron and hole wave functions. Furthermore, the magnitude of the signal from the $MoSe_2$ ML is proportional to the pump fluence (F), as shown in Figure 3f. A saturation effect is observed in the heterostructure sample, with the magnitude of the signal $\propto F/(1 + F/F_s)$, with a saturation fluence of F_s = 6.9 μJ cm^{-2} (black curve).

Finally, we explore a configuration illustrated in Figure 4a, where a 395 nm pump is used to excite both layers (blue vertical arrow), with a 655 nm probe tuned to the MoS_2 exciton resonance (red vertical arrow). We expect the electrons (holes) injected in $MoSe_2$ (MoS_2) transfer to MoS_2 ($MoSe_2$) layer rapidly, followed by formation and recombination of indirect excitons. This configuration also allows us to directly compare the heterostructure region with the MoS_2 ML region. Panels b and c of Figure 4 show the differential reflection signals measured with a pump fluence of 1 μJ cm^{-2} from the heterostructure (purple squares) and the MoS_2 ML (blue circles) for two time ranges, respectively. In both samples, the signal reaches a peak immediately after the pump excitation. After a subpicosecond fast decay process, the long-term decay process is bi-exponential in both samples. The two decay constants

as a function of the pump fluence are summarized in Figure 4d,e. Due to the relatively large uncertainty in the biexponential fits, we are unable to conclusively deduce how these constants change with the pump fluence. However, it is clear that both decay constants are longer in the heterostructure than the MoS_2 ML, under the same conditions. This is consistent with the expected longer lifetime of indirect excitons. Furthermore, saturation effects are observed in both samples, as indicated by the black curves in Figure 4f. Under the same conditions, the signal from the heterostructure is about twice larger than the MoS_2 ML. This is another evidence of electron transfer, since without such a process, the electrons excited in $MoSe_2$ would not contribute to the signal. In the heterostructure, the $MoSe_2$ layer donates electrons to MoS_2 but captures holes from it. Hence, the larger signal in the heterostructure also suggests that the electrons are more efficient in inducing a differential reflection signal than the holes in the same layer. We also note, by comparing Figures 4f and 2f, that the 395 nm pump generates a signal of about 5 times larger than the 790 nm pump in the heterostructure sample, with the same fluence. This can be attributed to the higher absorption of $MoSe_2$ and additional absorption of MoS_2 layers of the 395 nm pump.

CONCLUSION

We obtain evidence of ultrafast charge separation and indirect exciton formation in a heterostructure formed by MoS_2 and $MoSe_2$ MLs. By selectively injecting excitons in the $MoSe_2$ layer and probing the MoS_2 layer, we find that the electrons in the excitons injected in $MoSe_2$ transfer to MoS_2 on a subpicosecond time scale. Similarly, holes in the excitons resonantly injected in MoS_2 are found to transfer to $MoSe_2$ on the same time scale. Once transferred, the electrons and holes form spatially indirect excitons with recombination lifetimes longer than the excitons in individual MLs. The strong PL quenching effect observed in heterostructures also indicates that the charge transfer is highly efficient.

METHODS

Flakes of MoS_2 and $MoSe_2$ are first mechanically exfoliated from bulk crystals onto clear and flexible polydimethylsiloxane (PDMS) substrates using adhesive tapes. Monolayer flakes are identified by optical contrasts with an optical microscope, and later confirmed by photoluminescence measurements. Next, a $MoSe_2$ ML flake is transferred from the PDMS substrate onto a silicon wafer capped with 90 nm of silicon dioxide, utilizing a micromanipulator. The sample is then thermally annealed at 200 °C for 2 h under a H_2−Ar (20−100 sccm) environment at a base pressure of about 3 Torr. Then, a MoS_2 monolayer flake is precisely transferred onto the $MoSe_2$ flakes. The heterostructure flake is then thermally annealed under the same conditions as mentioned above.

In the differential reflection setup, the output of a diode laser with a wavelength of 532 nm and a power of 10 W is used to pump a Ti:sapphire laser, which generates 100 fs pulses with a central wavelength of 790 nm, a repetition rate of about 80 MHz, and an average power of 2 W. A small portion (about 8%) of this beam is reflected to a beta barium borate (BBO) crystal to generate its second harmonic at 395 nm. A dichroic beamsplitter is used after the BBO crystal to separate the 395 nm beam from the residual 790 nm beam. Both beams are used in the measurement. The majority of the 790 nm beam is incident to an optical parametric oscillator, which generates an output beam that is tunable around 1300 nm. Another BBO crystal is used to generate second harmonic of this beam around 650 nm. In the measurements, different combinations of these three beams (395 nm, 790 nm, and the tunable one around 650 nm) are used in different configurations.

In each configuration of the measurements, the selected pump and probe beams are combined by a beamsplitter and focused to the sample by a microscope objective lens with a numerical aperture of 0.4. The pump and probe spots are 1−2 μm in full-width at half-maxima. The reflection of the probe from the sample is collimated by the objective lens and is sent to a biased silicon photodiode. The reflected pump is prevented from reaching the detector by a set of filters. The output of the photodiode is measured by a lock-in amplifier, with the intensity of the pump beam modulated at about 2 kHz by a mechanical chopper. The differential reflection is measured as a function of the probe delay, which is controlled by the length of the pump path with a linear motor stage. In all the measurements, the pump and probe beams are linearly polarized along perpendicular directions.

Conflict of Interest: The authors declare no competing financial interest.

Acknowledgment. This material is based upon work supported by the National Science Foundation of USA under Award Nos. DMR-0954486 and IIA-1430493, the Kansas NSF EPSCoR First Award (EPS-0903806), and startup funding by The University of Kansas.

REFERENCES AND NOTES

1. von Klitzing, K. The Quantized Hall Effect. *Rev. Mod. Phys.* **1986**, *58*, 519–531.
2. König, M.; Wiedmann, S.; Brüne, C.; Roth, A.; Buhmann, H.; Molenkamp, L. W.; Qi, X. L.; Zhang, S. C. Quantum Spin Hall Insulator State in HgTe Quantum Wells. *Science* **2007**, *318*, 766–770.
3. Kasprzak, J.; Richard, M.; Kundermann, S.; Baas, A.; Jeambrun, P.; Keeling, J. M. J.; Marchetti, F. M.; Szymanska, M. H.; Andre, R.; Staehli, J. L.; *et al.* Bose−Einstein Condensation of Exciton Polaritons. *Nature* **2006**, *443*, 409–414.
4. Alferov, Z. I. Nobel Lecture: The Double Heterostructure Concept and Its Applications in Physics, Electronics, and Technology. *Rev. Mod. Phys.* **2001**, *73*, 767–782.
5. Novoselov, K. S.; Geim, A. K.; Morozov, S. V.; Jiang, D.; Zhang, Y.; Dubonos, S. V.; Grigorieva, I. V.; Firsov, A. A. Electric Field Effect in Atomically Thin Carbon Films. *Science* **2004**, *306*, 666–669.
6. Novoselov, K. S.; Geim, A. K.; Morozov, S. V.; Jiang, D.; Katsnelson, M. I.; Grigorieva, I. V.; Dubonos, S. V.; Firsov, A. A. Two-Dimensional Gas of Massless Dirac Fermions in Graphene. *Nature* **2005**, *438*, 197–200.
7. Song, L.; Ci, L. J.; Lu, H.; Sorokin, P. B.; Jin, C. H.; Ni, J.; Kvashnin, A. G.; Kvashnin, D. G.; Lou, J.; Yakobson, B. I. Large Scale Growth and Characterization of Atomic Hexagonal Boron Nitride Layers. *Nano Lett.* **2010**, *10*, 3209–3215.
8. Wang, Q. H.; Kalantar-Zadeh, K.; Kis, A.; Coleman, J. N.; Strano, M. S. Electronics and Optoelectronics of Two-Dimensional Transition Metal Dichalcogenides. *Nat. Nanotechnol.* **2012**, *7*, 699–712.

9. Geim, A. K.; Grigorieva, I. V. Van der Waals Heterostructures. *Nature* **2013**, *499*, 419–425.
10. Chuang, S.; Kapadia, R.; Fang, H.; Chang, T. C.; Yen, W. C.; Chueh, Y. L.; Javey, A. Near-Ideal Electrical Properties of InAs/WSe_2 van der Waals Heterojunction Diodes. *Appl. Phys. Lett.* **2013**, *102*, 242101.
11. Haigh, S. J.; Gholinia, A.; Jalil, R.; Romani, S.; Britnell, L.; Elias, D. C.; Novoselov, K. S.; Ponomarenko, L. A.; Geim, A. K.; Gorbachev, R. Cross-Sectional Imaging of Individual Layers and Buried Interfaces of Graphene-Based Heterostructures and Superlattices. *Nat. Mater.* **2012**, *11*, 764–767.
12. Gong, Y. J.; Yang, S. B.; Zhan, L.; Ma, L. L.; Vajtai, R.; Ajayan, P. M. A Bottom-Up Approach to Build 3D Architectures from Nanosheets for Superior Lithium Storage. *Adv. Funct. Mater.* **2014**, *24*, 125–130.
13. Britnell, L.; Gorbachev, R. V.; Jalil, R.; Belle, B. D.; Schedin, F.; Mishchenko, A.; Georgiou, T.; Katsnelson, M. I.; Eaves, L.; Morozov, S. V. Field-Effect Tunneling Transistor Based on Vertical Graphene Heterostructures. *Science* **2012**, *335*, 947–950.
14. Georgiou, T.; Jalil, R.; Belle, B. D.; Britnell, L.; Gorbachev, R. V.; Morozov, S. V.; Kim, Y. J.; Gholinia, A.; Haigh, S. J.; Makarovsky, O. Vertical Field-Effect Transistor Based on Graphene-WS_2 Heterostructures for Flexible and Transparent Electronics. *Nat. Nanotechnol.* **2013**, *8*, 100–103.
15. Lin, Y. F.; Li, W. W.; Li, S. L.; Xu, Y.; Aparecido-Ferreira, A.; Komatsu, K.; Sun, H. B.; Nakaharai, S.; Tsukagoshi, K. Barrier Inhomogeneities at Vertically Stacked Graphene-Based Heterostructures. *Nanoscale* **2014**, *6*, 795–799.
16. Yu, W. J.; Li, Z.; Zhou, H. L.; Chen, Y.; Wang, Y.; Huang, Y.; Duan, X. F. Vertically Stacked Multi-Heterostructures of Layered Materials for Logic Transistors and Complementary Inverters. *Nat. Mater.* **2013**, *12*, 246–252.
17. Bertolazzi, S.; Krasnozhon, D.; Kis, A. Nonvolatile Memory Cells Based on MoS_2/Graphene Heterostructures. *ACS Nano* **2013**, *7*, 3246–3252.
18. Shih, C. J.; Wang, Q. H.; Son, Y.; Jin, Z.; Blankschtein, D.; Strano, M. S. Tuning On-Off Current Ratio and Field-Effect Mobility in a MoS_2-Graphene Heterostructure *via* Schottky Barrier Modulation. *ACS Nano* **2014**, *8*, 5790–5798.
19. Kwak, J. Y.; Hwang, J.; Calderon, B.; Alsalman, H.; Munoz, N.; Schutter, B.; Spencer, M. G. Electrical Characteristics of Multilayer MoS_2 FET's with MoS_2/Graphene Heterojunction Contacts. *Nano Lett.* **2014**, *14*, 4511–4516.
20. Larentis, S.; Tolsma, J. R.; Fallahazad, B.; Dillen, D. C.; Kim, K.; Mac Donald, A. H.; Tutuc, E. Band Offset and Negative Compressibility in Graphene-MoS_2 Heterostructures. *Nano Lett.* **2014**, *14*, 2039–2045.
21. Choi, M. S.; Lee, G. H.; Yu, Y. J.; Lee, D. Y.; Lee, S. H.; Kim, P.; Hone, J.; Yoo, W. J. Controlled Charge Trapping by Molybdenum Disulphide and Graphene in Ultrathin Heterostructured Memory Devices. *Nat. Commun.* **2013**, *4*, 1624.
22. Bernardi, M.; Palummo, M.; Grossman, J. C. Extraordinary Sunlight Absorption and One Nanometer Thick Photovoltaics Using Two-Dimensional Monolayer Materials. *Nano Lett.* **2013**, *13*, 3664–3670.
23. Britnell, L.; Ribeiro, R. M.; Eckmann, A.; Jalil, R.; Belle, B. D.; Mishchenko, A.; Kim, Y.-J.; Gorbachev, R. V.; Georgiou, T.; Morozov, S. V. Strong Light-Matter Interactions in Heterostructures of Atomically Thin Films. *Science* **2013**, *340*, 1311–1314.
24. Yu, W. J.; Liu, Y.; Zhou, H.; Yin, A.; Li, Z.; Huang, Y.; Duan, X. Highly Efficient Gate-Tunable Photocurrent Generation in Vertical Heterostructures of Layered Materials. *Nat. Nanotechnol.* **2013**, *8*, 952–958.
25. Roy, K.; Padmanabhan, M.; Goswami, S.; Sai, T. P.; Ramalingam, G.; Raghavan, S.; Ghosh, A. Graphene-MoS_2 Hybrid Structures for Multifunctional Photoresponsive Memory Devices. *Nat. Nanotechnol.* **2013**, *8*, 826–830.
26. He, J.; Kumar, N.; Bellus, M. Z.; Chiu, H. Y.; He, D.; Wang, Y.; Zhao, H. Electron Transfer and Coupling in Graphene-Tungsten Disulfide van der Waals Heterostructures. *Nat. Commun.* **2014**, *5*, 5622.
27. Xu, H.; Wu, J.; Feng, Q.; Mao, N.; Wang, C.; Zhang, J. High Responsivity and Gate Tunable Graphene-MoS_2 Hybrid Phototransistor. *Small* **2014**, *10*, 2300–2306.
28. Wi, S. J.; Chen, M. K.; Nam, H.; Liu, A. C.; Meyhofer, E.; Liang, X. G. High Blue-Near Ultraviolet Photodiode Response of Vertically Stacked Graphene-MoS_2-Metal Heterostructures. *Appl. Phys. Lett.* **2014**, *104*, 232103.
29. Zhang, W. J.; Chuu, C. P.; Huang, J. K.; Chen, C. H.; Tsai, M. L.; Chang, Y. H.; Liang, C. T.; Chen, Y. Z.; Chueh, Y. L.; He, J. H. Ultrahigh-Gain Photodetectors Based on Atomically Thin Graphene-MoS_2 Heterostructures. *Sci. Rep.* **2014**, *4*, 3826.
30. Shi, Y. M.; Zhou, W.; Lu, A. Y.; Fang, W. J.; Lee, Y. H.; Hsu, A. L.; Kim, S. M.; Kim, K. K.; Yang, H. Y.; Li, L. J. Van der Waals Epitaxy of MoS_2 Layers using Graphene as Growth Templates. *Nano Lett.* **2012**, *12*, 2784–2791.
31. Lin, Y. C.; Lu, N.; Perea-Lopez, N.; Li, J.; Lin, Z.; Peng, X.; Lee, C. H.; Sun, C.; Calderin, L.; Browning, P. N. Direct Synthesis of van der Waals Solids. *ACS Nano* **2014**, *8*, 3715–3723.
32. Shim, G. W.; Yoo, K.; Seo, S. B.; Shin, J.; Jung, D. Y.; Kang, I. S.; Ahn, C. W.; Cho, B. J.; Choi, S. Y. Large-Area Single-Layer $MoSe_2$ and Its van der Waals Heterostructures. *ACS Nano* **2014**, *8*, 6655–6662.
33. Mak, K. F.; Lee, C.; Hone, J.; Shan, J.; Heinz, T. F. Atomically Thin MoS_2: A New Direct-Gap Semiconductor. *Phys. Rev. Lett.* **2010**, *105*, 136805.
34. Splendiani, A.; Sun, L.; Zhang, Y.; Li, T.; Kim, J.; Chim, C. Y.; Galli, G.; Wang, F. Emerging Photoluminescence in Monolayer MoS_2. *Nano Lett.* **2010**, *10*, 1271–1275.
35. Kosmider, K.; Fernandez-Rossier, J. Electronic Properties of the MoS_2-WS_2 Heterojunction. *Phys. Rev. B* **2013**, *87*, 075451.
36. Komsa, H. P.; Krasheninnikov, A. V. Electronic Structures and Optical Properties of Realistic Transition Metal Dichalcogenide Heterostructures from First Principles. *Phys. Rev. B* **2013**, *88*, 085318.
37. Kang, J.; Tongay, S.; Zhou, J.; Li, J. B.; Wu, J. Q. Band Offsets and Heterostructures of Two-Dimensional Semiconductors. *Appl. Phys. Lett.* **2013**, *102*, 012111.
38. Gong, C.; Zhang, H. J.; Wang, W. H.; Colombo, L.; Wallace, R. M.; Cho, K. J. Band Alignment of Two-Dimensional Transition Metal Dichalcogenides: Application in Tunnel Field Effect Transistors. *Appl. Phys. Lett.* **2013**, *103*, 053513.
39. Terrones, H.; Lopez-Urias, F.; Terrones, M. Novel Hetero-Layered Materials with Tunable Direct Band Gaps by Sandwiching Different Metal Disulfides and Diselenides. *Sci. Rep.* **2013**, *3*, 1549.
40. He, J. G.; Hummer, K.; Franchini, C. Stacking Effects on the Electronic and Optical Properties of Bilayer Transition Metal Dichalcogenides MoS_2, $MoSe_2$, WS_2, and WSe_2. *Phys. Rev. B* **2014**, *89*, 075409.
41. Lu, N.; Guo, H. Y.; Li, L.; Dai, J.; Wang, L.; Mei, W. N.; Wu, X. J.; Zeng, X. C. $MoS2_2$/MX_2 Heterobilayers: Bandgap Engineering *via* Tensile Strain or External Electrical Field. *Nanoscale* **2014**, *6*, 2879–2886.
42. Lu, N.; Guo, H.; Wang, L.; Wu, X.; Zeng, X. C. Van der Waals Trilayers and Superlattices: Modification of Electronic Structures of MoS_2 by Intercalation. *Nanoscale* **2014**, *6*, 4566–4571.
43. Fang, H.; Battaglia, C.; Carraro, C.; Nemsak, S.; Ozdol, B.; Kang, J. S.; Bechtel, H. A.; Desai, S. B.; Kronast, F.; Unal, A. A. Strong Interlayer Coupling in van der Waals Heterostructures Built From Single-Layer Chalcogenides. *Proc. Natl. Acad. Sci. U.S.A.* **2014**, *111*, 6198–6202.
44. Furchi, M. M.; Pospischil, A.; Libisch, F.; Burgdorfer, J.; Mueller, T. Photovoltaic Effect in an Electrically Tunable van der Waals Heterojunction. *Nano Lett.* **2014**, *14*, 4785–4791.
45. Roy, T.; Tosun, M.; Kang, J. S.; Sachid, A. B.; Desai, S. B.; Hettick, M.; Hu, C. C.; Javey, A. Field-Effect Transistors Built From All Two-Dimensional Material Components. *ACS Nano* **2014**, *8*, 6259–6264.
46. Hong, X.; Kim, J.; Shi, S. F.; Zhang, Y.; Jin, C.; Sun, Y.; Tongay, S.; Wu, J.; Zhang, Y.; Wang, F. Ultrafast Charge Transfer in Atomically Thin MoS_2/WS_2 Heterostructures. *Nat. Nanotechnol.* **2014**, *9*, 682–686.

47. Rivera, P.; Schaibley, J. R.; Jones, A. M.; Ross, J. S.; Wu, S.; Aivazian, G.; Klement, P.; Ghimire, N. J.; Yan, J.' Mandrus, D. G. Observation of Long-Lived Interlayer Excitons in Monolayer $MoSe_2$-WSe_2 Heterostructures. Preprint **2014**, ArXiv:1403.4985.
48. Tongay, S.; Zhou, J.; Ataca, C.; Lo, K.; Matthews, T. S.; Li, J. B.; Grossman, J. C.; Wu, J. Q. Thermally Driven Crossover From Indirect Toward Direct Bandgap in 2D Semiconductors: MoS_2 *versus* $MoSe_2$. *Nano Lett.* **2012**, *12*, 5576–5580.
49. Ross, J. S.; Wu, S.; Yu, H.; Ghimire, N. J.; Jones, A. M.; Aivazian, G.; Yan, J.; Mandrus, D. G.; Xiao, D.; Yao, W. Electrical Control of Neutral and Charged Excitons in a Monolayer Semiconductor. *Nat. Commun.* **2013**, *4*, 1474.
50. Tonndorf, P.; Schmidt, R.; Bottger, P.; Zhang, X.; Borner, J.; Liebig, A.; Albrecht, M.; Kloc, C.; Gordan, O.; Zahn, D. R. T. Photoluminescence Emission and Raman Response of Monolayer MoS_2, $MoSe_2$, and WSe_2. *Opt. Express* **2013**, *21*, 4908.
51. Kozawa, D.; Kumar, R.; Carvalho, A.; Amara, K. K.; Zhao, W.; Wang, S.; Toh, M.; Ribeiro, R. M.; Castro Neto, A. H.; Matsuda, K. Photocarrier Relaxation Pathway in Two-Dimensional Semiconducting Transition Metal Dichalcogenides. *Nat. Commun.* **2014**, *5*, 4543.
52. Kumar, N.; Cui, Q.; Ceballos, F.; He, D.; Wang, Y.; Zhao, H. Exciton-Exciton Annihilation in $MoSe_2$ Monolayers. *Phys. Rev. B* **2014**, *89*, 125427.
53. Sun, D.; Rao, Y.; Reider, G. A.; Chen, G.; You, Y.; Brezin, L.; Harutyunyan, A. R.; Heinz, T. F. Observation of Rapid Exciton-Exciton Annihilation in Monolayer Molybdenum Disulfide. *Nano Lett.* **2014**, *14*, 5625.